Fully permanent magnet atom chip for Bose-Einstein condensation

T. Fernholz,[1,*] R. Gerritsma,[1,†] S. Whitlock,[1,2] I. Barb,[1] and R. J. C. Spreeuw[1]

[1]*Van der Waals-Zeeman Institute, University of Amsterdam, Valckenierstraat 65, 1018 XE Amsterdam, Netherlands*
[2]*ARC Centre of Excellence for Quantum-Atom Optics and Centre for Atom Optics and Ultrafast Spectroscopy,*
Swinburne University of Technology, Hawthorn, Victoria 3122, Australia

We describe a proof-of-principle experiment on a fully permanent magnet atom chip. We study ultracold atoms and produce a Bose-Einstein condensate. The magnetic trap is loaded efficiently by adiabatic transport of a magnetic trap via the application of uniform external fields. Radio frequency spectroscopy is used for in-trap analysis and to determine the temperature of the atomic cloud. The formation of a Bose-Einstein condensate is observed in time-of-flight images and as a narrow peak appearing in the radio frequency spectrum.

I. INTRODUCTION

Miniature patterns of magnetic field sources integrated on planar substrates, atom chips, are used to manipulate magnetically trapped clouds of ultracold neutral atoms [1–4]. Atom chips based on current-carrying wires are relatively simple and versatile tools, readily used to produce Bose-Einstein condensates (BEC) [5,6]. Subsequently a wide range of experiments have been performed; for example, BECs can be precisely positioned with atomic conveyer-belt potentials [5,7], and phase-coherent splitting and interference of condensates has been achieved using double-well potentials [8,9].

Atom chips can also incorporate permanent magnetic materials [10–14], with significant additional advantages over current-carrying wires alone. Specifically, permanent magnet atom chips do not suffer from current noise which is partly responsible for trap loss and heating of atoms near conducting surfaces [10]. They are also well suited for tightly confining trapping potentials without the technical problems associated with high current densities. Furthermore, patterned permanent magnetic materials provide greater design freedom, allowing complex magnetic potentials to be realized such as ring-shaped waveguides or large two-dimensional arrays of microtraps [15–17].

One obvious drawback of permanent magnets however is the relatively limited degree of dynamic control available over the associated trapping potentials. The permanent magnetic field is a particular source of difficulty when loading the atom chip. As such, most permanent magnetic structures rely on current carrying wires to load and to complete the permanent magnetic trapping potential. Analysis is another complication, because standard techniques such as free ballistic expansion are impossible in the permanent magnetic field. These basic challenges need to be addressed before more sophisticated atom chip designs incorporating permanent magnets can be realized.

In this paper we describe the loading of ultracold atoms and evaporative cooling used to produce a BEC in a fully permanent magnetic microtrap, without additional external control fields. Although the permanent magnetic chip is in principle "self-biasing" we use a small field derived from an externally installed permanent magnet to tune the Ioffe field of the trap. To load the permanent magnet trap we adiabatically transfer the atoms to the chip surface from a quadrupole magnetic trap by applying a combination of bias magnetic fields. During loading we apply a radio frequency field to evaporatively cool the cloud. Analysis of the cloud temperature and spectral distribution is then performed using radio frequency spectroscopy [18–23]. This technique is also used to observe the BEC transition *in-situ* without expansion from the trap. It is also possible to eject the cloud from the self-biased trap by rapidly switching on uniform magnetic fields to observe the BEC transition using conventional absorption imaging.

II. SETUP

Our atom chip consists of a F-shaped permanent magnet structure (Fig. 1), designed to produce a self-biased Ioffe-Pritchard microtrap 180 μm from the chip surface [12,24]. It is cut from 40 μm thick FePt foil by computer numerical controlled (CNC) spark erosion and is glued to an aluminum-coated glass substrate. The magnetization is oriented in-plane along the y direction and was measured using superconducting quantum interference devices magnetometry as 430
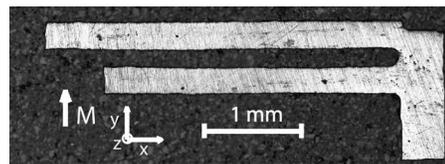
*Present address: QUANTOP, Danish Quantum Optics Center, Niels Bohr Institute, 2100 Copenhagen, Denmark; fernholz@nbi.dk

†Present address: Institut für Quantenoptik und Quanteninformation der Österreichischen Akademie der Wissenschaften, Otto-Hittmair-Platz 1, A-6020 Innsbruck, Austria.

FIG. 1. Permanent magnetic structure for producing a Ioffe trap 180 μm above the surface. The structure has a thickness of 40 μm and an in-plane magnetization of 430 kA/m.

kA/m. Assuming a uniform magnetization, we calculate an anisotropic, harmonic trapping potential with trapping frequencies of $2\pi \times 11$ kHz and $2\pi \times 30$ Hz in the radial and axial directions respectively. The calculated magnetic field at the trap minimum (Ioffe field) is 1 G, in the x direction.

It was found experimentally that uncompensated stray fields, such as the earth magnetic field in combination with field corrugation caused by the coarseness of the magnetic structure, added field components in the x direction on the order of 2 G. The design aimed at a rather low Ioffe field to achieve tight radial confinement, making it necessary to tune the Ioffe field to a higher value to avoid field zeros in the trap. This was done with an externally installed permanent magnet, thus preserving the permanent magnetic nature of the trap. The permanent magnet was placed on the optical table (≈ 25 cm below the chip), adding a homogeneous field of ≈ 4 G in the x direction. The trap frequencies in the lowest minimum were then measured to be $2\pi \times 5.2$ kHz radial and $2\pi \times 128$ Hz axial with a field minimum around 2.7 G. Due to the field corrugation, the axial confinement is significantly larger than expected. We attribute the field corrugation mainly to the rather unsophisticated production of the chip and feel that a more advanced atom chip (for instance, produced with patterning techniques based on optical lithography) could be fully self-biased. We note that in fact it was possible to load a secondary axial minimum of the trap and perform evaporative cooling without the permanent magnet installed, but less efficiently.

The atom chip is mounted upside down in a quartz-cell vacuum chamber ($4 \times 4 \times 7$ cm^3), which is surrounded by three orthogonal coil pairs that can produce magnetic fields >100 G with any desired polarity. The coils are used to load the atoms into the permanent magnet trap as described below. The loading procedure ends by ramping the currents to zero and short-circuiting the coils with relays. The latter significantly reduces the residual magnetic field noise. Additional sources of magnetic field noise, such as the current supplies themselves, were identified and placed >5 m from the experiment. Residual background field noise at 50 Hz was further reduced by feeding a phase and amplitude adjusted 50 Hz signal derived from the mains to a large coil pair placed around the experiment. Our efforts reduced the root-mean-square magnetic field noise in the x direction from more than 20 mG to below 0.5 mG. Radio frequency (rf) fields used for forced evaporative cooling and for rf spectroscopy of the atom cloud are produced by a computer controlled 10-bit direct digital synthesis rf generator [25] (AD9959) with four independent outputs. We use two outputs connected to separate antennas for evaporative cooling and rf spectroscopy.

III. LOADING PROCEDURE

In this section we describe the loading process of the permanent magnetic trap using external uniform bias fields. The possibilities and restrictions for moving magnetic traps by this method have been described in detail in [26]. Efficiently loading atoms into the trap proves to be nontrivial since at the end of the loading procedure all external fields should be
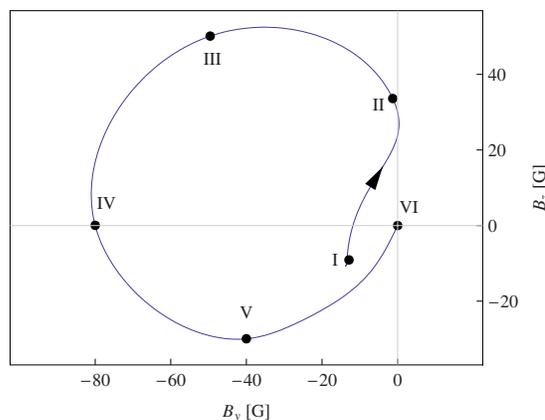

FIG. 2. (Color online) Homogeneous magnetic field components applied during the loading process. Position I corresponds to the initial coil based quadrupole trap. The magnetic field zero is moved close to the chip and the anti-Helmholtz coils are subsequently turned off near position II, turning the trap into a Ioffe trap. This trap is then moved toward the final location, replacing the initial self-biased trap. All fields are turned off at position VI.

turned off. The main difficulty arises from the already present field minimum, located close to the chip, containing no atoms at the start of the loading process. This minimum can act as a leak when the trap containing the atoms is brought too close to it. We have optimized a particular loading trajectory that avoids this secondary minimum as much as possible. Another important feature is that the magnetic field minimum is kept above zero during the last part of the loading process, making it possible to evaporatively cool during the transfer without significant loss due to Majorana spin-flip transitions.

We collect approximately 7×10^7 ^{87}Rb atoms in a mirror magneto-optical trap (MOT). The MOT is made with the help of external field coils, at a distance of 8 mm from the surface where the field of the chip is negligible. The atomic cloud is then compressed (CMOT) and optically pumped to the magnetically trappable $|F=2, m_F=2\rangle$ state. After switching all laser beams off, the cloud is trapped 8 mm below the chip surface using the quadrupole magnetic field produced by one pair of coils operated in anti-Helmholtz configuration. Additional uniform fields can bring this trap closer to the chip. In close proximity to the chip surface the field gradient produced by the F-shaped magnet is large enough to hold the atoms against gravity and the anti-Helmholtz coils can be turned off. At this point two magnetic field minima exist. A weak trap containing the atoms is produced by the magnet in combination with a uniform bias field and is located far from the chip surface. A tighter trap close to the chip surface also originates from the magnet and is at this point still vacant.

An efficient method to transfer atoms to the permanent magnetic trap is to move the atoms to the location of the final trap while avoiding the secondary trap. We use a time ordered sequence of uniform magnetic fields in the y and z directions as shown in Fig. 2. The merging of the two minima is prevented through an additional B_z component of the applied field. The B_z component is then inverted, as shown in Fig. 2, moving the trap containing the atoms to-

ward the chip, while the empty trap retreats. Finally, after ramping the fields off, the atom cloud is left in the permanent magnetic trap.

Three-dimensional calculations of the magnetic field isosurfaces during the loading are shown in Fig. 3 (II–VI). During this transfer the magnetic field gradient of the filled trap increases from ~60 G/cm to ~6800 G/cm which leads to significant heating of the atom cloud. Although the two field minima do not merge, they pass each other separated by a finite potential barrier of ~15 G which allows energetic atoms to spill over to the decompressing trap. This loss mechanism can take away up to 80% of the magnetically trapped atoms. However, it has been possible to load 2×10^6 atoms into the permanent magnet trap. A series of absorption images at various detunings is taken during the loading in order to create a series of optical spectra of the trapped cloud and is shown in Fig. 4. The observed atom distributions compare very well with the calculated field distributions in Fig. 3. The cloud temperature inferred from the optical spectrum in the self-biased trap is approximately $T \approx 1$ mK, yielding a peak phase space density of $\rho = N(\hbar\bar{\omega}/k_B T)^3 \approx 8 \times 10^{-7}$. Here, N is the atom number, $\hbar = h/2\pi$ is Planck's constant, $\bar{\omega}$ is the geometrical mean trap frequency, and k_B is the Boltzmann factor.

To improve the starting conditions for the final evaporation stage and to avoid loss due to the finite barrier height we apply forced radio frequency evaporative cooling already during the compression of the trap. Evaporative cooling, however, requires a trap with nonzero minimum to prevent spin-flip loss. We choose a trajectory that always maintains a nonzero minimum during the final approach of the atomic cloud. It is nontrivial that such a trajectory exists [26]. We have found that the trap turns into a Ioffe trap after the turn off of the anti-Helmholtz coils and remains a Ioffe trap during the rest of the loading process (steps II–VI in Fig. 3). The preliminary evaporative cooling stage during the transfer consists of a 6 s linear rf ramp from 35 MHz to 8 MHz. At the end of the ramp all externally controlled fields are turned to zero and the cloud is trapped in the potential produced by the magnetic structures alone. After loading, the cloud contains approximately 10^5 atoms at a temperature of 60 μK yielding a peak phase space density of $\rho \approx 2 \times 10^{-4}$. Although the number of atoms is relatively small, the high trap frequencies result in a mean collision rate of ~200 s^{-1}. A final rf evaporative cooling stage is performed with a linear rf sweep over 2.3 s from 8 MHz down to ~1.9 MHz which lowers the trap depth from 600 μK to 10 μK.

IV. RADIO FREQUENCY SPECTROSCOPY

The most commonly used diagnostic technique for ultracold atoms is free ballistic expansion followed by absorption imaging. In our case this is not possible due to the permanent character of the magnetization of our chip. Instead, we employ radio frequency spectroscopy to characterize the ultracold atom cloud in the permanent magnetic trap. This allows us to directly probe the energy distribution of the confined cloud and to extract the cloud temperature without ballistic expansion.

The cloud is probed by applying a radio frequency pulse of frequency f for a duration of 0.5 ms. Trapped atoms satisfying the resonant condition $hf = g_F \mu_B B(x,y,z)$ may be coupled to untrapped magnetic states and are then immediately lost from the trap. Here, g_F is the atomic Landé factor, μ_B is the Bohr magneton, and B is the local magnetic field modulus. We measure the number of lost atoms by applying a magnetic field of 25 G in the y direction to push the atoms away from the chip surface and to weaken the trapping potential for detection. Resonant absorption imaging can then provide an accurate measure of the number of remaining atoms.

In Fig. 5 radio frequency spectra are shown for various final evaporation frequencies. Above the BEC transition temperature T_c, we can fit a theoretical model to the radio frequency spectra to obtain the temperature of the cloud, whereas below T_c radio frequency spectroscopy can be used to observe the BEC transition without free expansion and to measure the chemical potential μ. The following sections describe both techniques.

A. Thermometry

If we assume that the atoms move through the resonant surface at a constant speed perpendicular to the surface, we can describe the spin-flip transition probability by the Landau-Zener expression [27,28]. To obtain a model for the loss rate spectrum we integrate the spin-flip probability over the velocity distribution and over the resonant surface. We introduce the radio frequency above the trap bottom $\omega_{\text{rf}} = 2\pi(f - f_0)$ and the thermal frequency $\omega_{\text{th}} = k_B T/\hbar$. In the case of a gas well above the condensation temperature $T \gg T_c$ we find that the loss rate in an isotropic trap is well described by

$$\frac{dN}{dt} \approx \left(\frac{1}{2\pi\Omega^2} + \frac{\sqrt{m_F}}{4\bar{\omega}\sqrt{\pi\omega_{\text{th}}\omega_{\text{rf}}}} \right)^{-1} n_{\omega_{\text{rf}}}, \tag{1}$$

where we introduced the resonant atomic spectral distribution $n_{\omega_{\text{rf}}} = dN/d\omega_{\text{rf}}$, using Boltzmann statistics:

$$n_{\omega_{\text{rf}}} = \frac{2N}{\sqrt{\pi}} \sqrt{\frac{m_F^3 \omega_{\text{rf}}}{\omega_{\text{th}}^3}} e^{-m_F \omega_{\text{rf}}/\omega_{\text{th}}}. \tag{2}$$

As it can be seen from Eq. (1), the loss rate becomes independent of the trapping parameters and reflects the potential energy distribution [Eq. (2)] for sufficiently small Rabi frequencies $\Omega^2 \ll \bar{\omega}\omega_{\text{th}}/\sqrt{m_F}$. This arises from the fact that the out-coupling rate becomes independent of the momentum distribution under the above assumptions.

For temperatures approaching T_c, Eq. (2) is no longer valid since it is based on Boltzmann statistics. For Bose-Einstein statistics we cannot evaluate the integrals to obtain an expression for dN/dt similar to Eq. (1). Instead we integrate the Landau-Zener probability numerically, including the trap anisotropy. To obtain the cloud temperature from our data, we fix μ using the measured atom number N by setting $\int n_{\omega_{\text{rf}}} d\omega_{\text{rf}} = N$. The results of this calculation are shown as solid lines in Fig. 5.
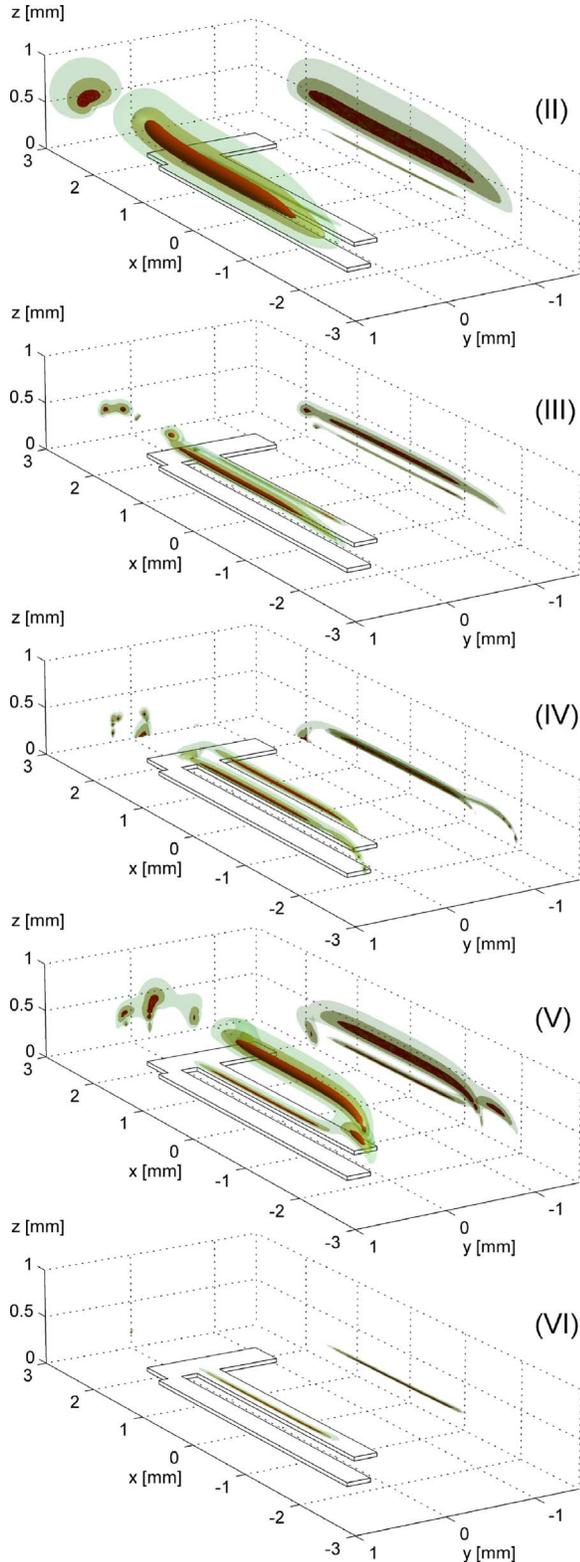
FIG. 3. (Color online) Simulated contours of magnetic field strength [corresponding to Fig. 2 (II–VI)] together with their x and y projections (red=8 G, green=16 G, blue=24 G) during the loading process. The filled trap on the left-hand side is compressed and moved toward the chip while the empty trap is decompressed, moves away from the chip, and disappears when the field is turned to zero (VI).
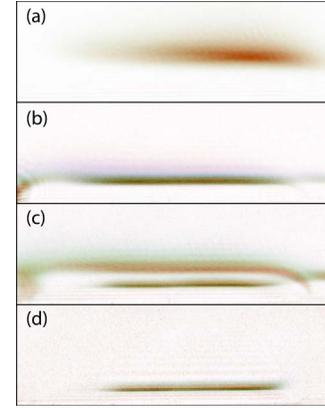

FIG. 4. (Color online) Spectrally colored absorption images taken during loading without evaporative cooling. The field of view is 3.6×1.7 mm². Every image is composed of several absorption images taken at 22 different probe detunings, ranging from 0 to 60 MHz. The absorption images are overlapped after mapping them onto a color code where red corresponds to 0 G Zeeman shift and blue to ~30 G Zeeman shift. (a)–(d) correspond to Fig. 3 (II, IV–VI). (d) corresponds to the loaded final trap with all externally controlled fields turned off.

We can alternatively assume that Eq. (1) also holds for Bose-Einstein statistics with the correct potential energy distribution (dashed lines in Fig. 5). For a noninteracting cloud with $T \gtrsim T_c$ the resonant spectral distribution is given by

$$n_{\omega_{\rm rf}} = 4 \frac{\sqrt{\pi m_F^3 \omega_{\rm th}^3 \omega_{\rm rf}}}{\overline{\omega}^3} g_{3/2} \big[e^{(\mu/\hbar - m_F \omega_{\rm rf})/\omega_{\rm th}} \big]. \tag{3}$$

Here $g_{3/2}(x)$ is the polylogarithm function with base 3/2, and μ is the chemical potential. The inferred temperatures devi-
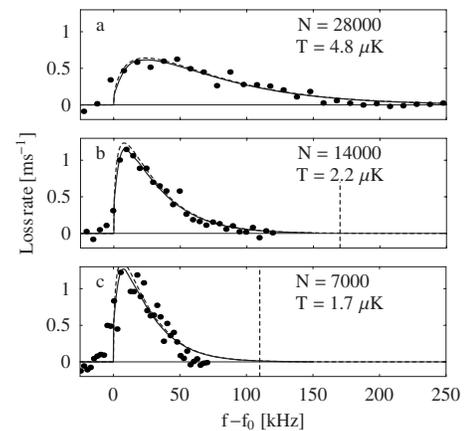

FIG. 5. Radio frequency spectra taken for various final evaporation frequencies of 370, 170, and 110 kHz above the trap bottom f_0, as indicated by the dashed vertical lines [(a)–(c), respectively]. The model used to describe the spectra is obtained by numerical integration of the Landau-Zener spin-flip probability assuming Bose-Einstein statistics (solid lines). The calculations consider the anisotropic trap geometry and give a Rabi frequency of $\Omega \approx 2\pi \times 0.8$ kHz. The dashed lines indicate the prediction of the potential energy model using Eq. (3) with the same parameters.
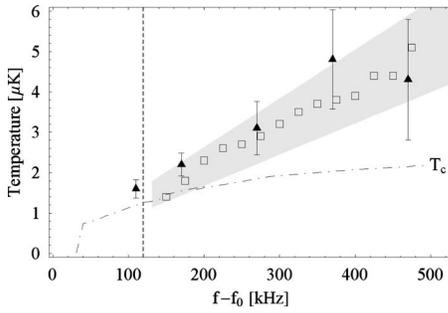
FIG. 6. Temperature inferred from the axial density distribution (▲) compared to temperature obtained from rf spectra (□) as a function of final evaporation radio frequency with respect to the trap bottom. The gray area gives the confidence interval for the temperature inferred from the axial density distribution, based on estimated systematic errors on the pixel size and lensing errors. The curve for T_c is obtained from the atom number and the trap frequencies, and is corrected for the finite size of the cloud [29]. The dashed line at 120 kHz corresponds to the observed onset of condensation.

ate by less than 15% from the numerically obtained results.

As an alternative temperature measurement we also observe the axial density distribution of the cloud in the trap. To avoid problems in the absorption imaging due to the high optical density of the cloud we lift the magnetic field at the trap bottom by 50 G to weaken the radial confinement, and detune the probe laser by 18 MHz to the blue of the σ^+ transition. By fitting the axial density distribution we obtain the temperature of the cloud.

In Fig. 6 we compare the temperatures found from spectra and the inferred temperature from the axial density distribution of the cloud for different final evaporation radio frequencies. Also shown is the confidence interval of the temperature based on the axial size. This interval is estimated for systematic errors such as lensing of the probe light by the dense cloud, pixel size calibration errors, and finite imaging resolution. The plot shows excellent agreement between the two temperature measurements.

B. Bose-Einstein condensation

To observe the onset of Bose-Einstein condensation we increased the probing time to 10 ms and decreased the radio frequency amplitude by a factor of 3 to minimize power broadening. It took considerable effort in magnetic field noise reduction to obtain the resolution needed to observe the narrow condensation peak. In addition, it was necessary to maintain the same cycle for the applied magnetic fields throughout the experiment to minimize hysteresis effects in the magnetic material and surrounding structures, which otherwise could lead to variations in the trap bottom of several 10 kHz. The observed spectra below T_c are shown in Fig. 7. Lowering the final radio frequency results in a bimodal spectrum and eventually in a spectrum of a nearly pure condensate with a width of ~5 kHz. This agrees well with the chemical potential derived from atom number and trap frequencies of $\mu/m_F h = 4.3$ kHz. Each spectrum is averaged 6 times and consists of about 70 data points, spread nonlin-
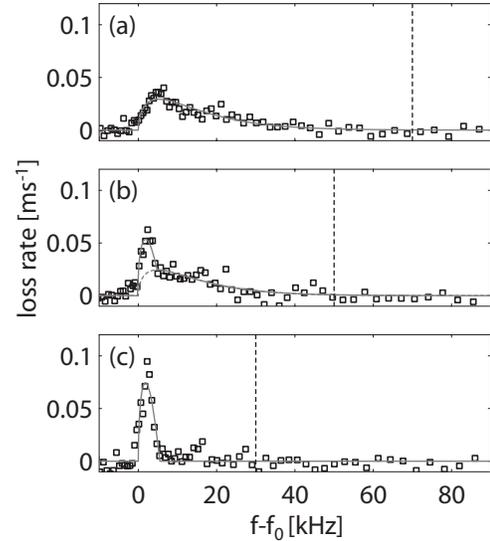

FIG. 7. Spectra of (a) a cloud close to T_c, (b) a partially condensed cloud, and (c) a nearly pure condensate. The dashed lines indicate the position of the final radio frequency cooling "knife" with respect to the trap bottom ($f_0 \approx 1.85$ MHz). The full width of the condensate spectrum is ~5 kHz, corresponding to the chemical potential $\mu/m_F h$. The bimodal fits, shown in light gray solid and dashed lines for the condensate and thermal part, respectively, are based on a heuristic model.

early over the spectral range to emphasize the bimodal nature and condensate peak.

V. EXPANSION

As an alternative way to identify the BEC transition, we ramp on, over 2 ms, a magnetic field of 50 G, which rapidly transfers the atom cloud 1 mm away from the chip surface. At this position all magnetic fields are suddenly switched off and the acquired kinetic energy of the atoms is sufficient to overcome the remaining potential barrier. The cloud is accelerated further by gravity and the rapidly decaying field of the chip. After 3.5 ms an absorption image is taken to reveal a partially expanded atom cloud (Fig. 8). As the final trap depth is reduced, the atom distribution becomes bimodal with a narrow central peak and a change in aspect ratio. Combining these absorption images with the radio frequency spectra we find the BEC transition at a trap depth of about 11 μK, with 7000 atoms at a temperature of $T_c \sim 1.6$ μK, which is close to the expected value of $T_c = 1.3$ μK. Continued evaporation results in a nearly pure BEC consisting of ~1500 atoms.

Although this ejection method is useful for observing the phase transition to BEC it cannot be reliably used to obtain temperatures because of the nonadiabatic nature of the expansion and the large magnetic field gradients during the expansion. It can however be used to obtain condensate fractions.

We observe strong heating of the ultracold cloud (~6 μK/s) during the final stage of evaporation. This is likely caused by three-body collisions as the estimated den-
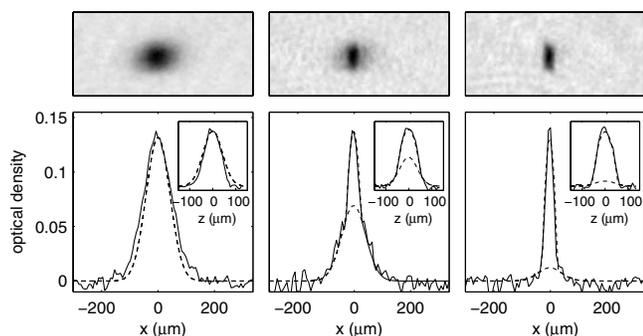
FIG. 8. Absorption images taken after expansion of the cloud (10 times averaged). The atoms are first taken out of the self-biased trap by field ramps. Then the fields are suddenly turned off and the cloud falls and expands for 3.5 ms. From left to right, the figures show a thermal cloud, a partly condensed cloud, and a nearly pure condensate of 1500 atoms, corresponding to final rf frequencies of 1970, 1920, and 1890 kHz. The lower graphs and insets show axial and radial cross sections, respectively, through the center of the cloud, with two-dimensional bimodal fits shown with dashed lines.

sity at the trap center near T_c is quite high, $n(0) \approx 6 \times 10^{14}$ cm^{-3}. As a result, the lifetime of the condensate is ~15 ms without a rf shield and ~150 ms with a rf shield [30,31]. The quoted density corresponds to a three-body decay rate of ~3 s^{-1} [31,32]. It is thus likely that three-body decay limits the final number of condensate atoms during the last evaporation stage.

It is interesting to note that condensation is observed in the expanded cloud at higher evaporation frequencies than in the rf spectra. We suspect this is because of the long rf probing time necessary to obtain the desired resolution and signal-to-noise ratio, causing considerable heating during the radio frequency pulse. It is also possible that the signal-to-noise ratio does not allow the observation of small conden-

sate fractions, because it requires the removal of a substantial fraction of atoms.

VI. CONCLUSIONS

In conclusion, we have presented solutions to the problems of loading and analysis of an atomic cloud on a fully permanent magnetic chip. We have demonstrated an efficient loading procedure relying on the adiabatic movement of Ioffe traps using uniform external fields, allowing the application of forced evaporative cooling during loading. After loading, radio frequency spectroscopy is used to characterize the cloud. A model is derived for fitting rf spectra to obtain cloud temperatures. The fitted temperatures compare well to temperatures derived from fitting the in-trap axial density distribution. Noise reduction and radio frequency power reduction give the resolution needed to observe the onset of Bose-Einstein condensation in radio frequency spectra. This results in bimodal spectra and eventually in a spectrum of a nearly pure condensate. Alternatively, condensation is observed by ejecting the atomic cloud by switching external magnetic fields. Together, these techniques have allowed us to analyze our atomic cloud in the permanent magnetic field.

[1] R. Folman *et al.*, Adv. At., Mol., Opt. Phys. **48**, 263 (2002).

[2] J. Reichel, Appl. Phys. B: Lasers Opt. **74**, 469 (2002).

[3] N. Dekker, C. S. Lee, V. Lorent, J. H. Thywissen, S. P. Smill, M. Drndić, R. M. Westervelt, and M. Prentiss, Phys. Rev. Lett. **84**, 1124 (2000).

[4] J. Fortagh and C. Zimmermann, Rev. Mod. Phys. **79**, 235 (2007).

[5] W. Hänsel, P. Hommelhoff, T. W. Hänsch, and J. Reichel, Nature (London) **413**, 498 (2001).

[6] H. Ott, J. Fortagh, G. Schlotterbeck, A. Grossmann, and C. Zimmermann, Phys. Rev. Lett. **87**, 230401 (2001).

[7] A. Günther, M. Kemmler, S. Kraft, C. J. Vale, C. Zimmermann, and J. Fortagh, Phys. Rev. A **71**, 063619 (2005).

[8] T. Schumm *et al.*, Nat. Phys. **1**, 57 (2005).

[9] G.-B. Jo, Y. Shin, S. Will, T. A. Pasquini, M. Saba, W. Ketterle, D. E. Pritchard, M. Vengalattore, and M. Prentiss, Phys. Rev. Lett. **98**, 030407 (2007).

[10] C. D. J. Sinclair, E. A. Curtis, I. L. Garcia, J. A. Retter, B. V. Hall, S. Eriksson, B. E. Sauer, and E. A. Hinds, Phys. Rev. A **72**, 031603(R) (2005).

[11] B. V. Hall *et al.*, J. Phys. B **39**, 27 (2006).

[12] I. Barb *et al.*, Eur. Phys. J. D **35**, 75 (2005).

[13] M. Boyd, E. Streed, P. Medley, G. Campbell, J. Mun, W. Ketterle, and D. Pritchard, Phys. Rev. A **76**, 043624 (2007).

[14] A. Shevchenko, M. Heilio, T. Lindvall, A. Jaakkola, I. Tittonen, M. Kaivola, and T. Pfau, Phys. Rev. A **73**, 051401(R) (2006).

[15] T. Fernholz, R. Gerritsma, P. Krüger, and R. J. C. Spreeuw, Phys. Rev. A **75**, 063406 (2007).

[16] S. Ghanbari, T. D. Kieu, A. Sidorov, and P. Hannaford, J. Phys. B **39**, 847 (2006).

[17] R. Gerritsma, S. Whitlock, T. Fernholz, H. Schlatter, J. A. Luigjes, J. U. Thiele, J. B. Goedkoop, and R. J. C. Spreeuw, Phys. Rev. A **76**, 033408 (2007).

[18] A. G. Martin, K. Helmerson, V. S. Bagnato, G. P. Lafyatis, and D. E. Pritchard, Phys. Rev. Lett. **61**, 2431 (1988).

[19] K. Helmerson, A. G. Martin, and D. E. Pritchard, J. Opt. Soc. Am. B **9**, 483 (1992).

[20] I. Bloch, T. W. Hänsch, and T. Esslinger, Phys. Rev. Lett. **82**, 3008 (1999).

[21] S. Gupta *et al.*, Science **300**, 1723 (2003).

[22] C. Chin *et al.*, Science **305**, 1128 (2004).

[23] S. Whitlock, B. V. Hall, T. Roach, R. Anderson, M. Volk, P. Hannaford, and A. I. Sidorov, Phys. Rev. A **75**, 043602 (2007).

[24] Y. T. Xing *et al.*, J. Magn. Magn. Mater. **313**, 192 (2007).

[25] O. Morizot *et al.*, e-print arXiv:0704.1974.

[26] R. Gerritsma and R. J. C. Spreeuw, Phys. Rev. A **74**, 043405 (2006).

[27] N. V. Vitanov and K.-A. Suominen, Phys. Rev. A **56**, R4377 (1997).

[28] C. Wittig, J. Phys. Chem. B **109**, 8428 (2005).

[29] W. Ketterle and N. van Druten, Phys. Rev. A **54**, 656 (1996).

[30] M. Mewes, M. R. Andrews, N. J. van Druten, D. M. Kurn, D. S. Durfee, and W. Ketterle, Phys. Rev. Lett. **77**, 416 (1996).

[31] E. A. Burt, R. W. Ghrist, C. J. Myatt, M. J. Holland, E. A. Cornell, and C. E. Wieman, Phys. Rev. Lett. **79**, 337 (1997).

[32] J. Söding *et al.*, Appl. Phys. B: Lasers Opt. **69**, 257 (1999).